SEA SURFACE KA-BAND DOPPLER SCATTEROMETRY AT HIGH WIND SPEED: A FIELD EXPERIMENT

Yury Yu. Yurovsky[1], Vladimir N. Kudryavtsev[2,1], Semyon A. Grodsky[3], and Bertrand Chapron[2,4]

[1]FSBSI FRC Marine Hydrophysical Institute RAS, 2, Kapitanskaya, Sevastopol 299011, Russia,
Email: yyyurovsky@gmail.com
[2]Russian State Hydrometeorological University, 98, Malookhtinskiy, Saint-Petersburg 195916, Russia,
Email: kudr@rshu.ru
[3]University of Maryland, Dept. of Atmospheric and Oceanic Sciences, College Park, MD 20742, USA,
Email: senya@umd.edu
[4]Institut Français de Recherche pour l'Exploitation de la Mer, Pointe du Diable, Plouzane 29280, France,
Email: bertrand.chapron@ifremer.fr

KEYWORDS: radar, scatterometer, Ka-band, ocean, Doppler

ABSTRACT: Measuring sea surface winds and currents from space may become possible using a Doppler scatterometer. Dedicated missions are planned in the Ka-band to improve the data resolution and accuracy. However, the knowledge of the Ka-band backscattering from the real sea surface is still poor. Particularly, the behavior of the Ka-band backscattered signal is less known for high wind conditions (>20m/s). The Ka-band cross-section, in contrast to the lower frequency Ku/X/C/L-bands, is more sensitive to small-scale particles, e.g. droplets separated from wave crests at high winds. In this message, we report the results of a tower-based field experiment conducted using a continuous wave dual-co-polarized Ka-band radar during strong, up to 33 m/s, offshore wind events. In addition to the radar, this strong offshore katabatic wind event, about 12 hours long, was also recorded by supplementary wave, wind, and current sensors. At the wave fetch about 1 km, the maximum wavelength was about 10 m. At such extremely young wind-sea conditions, an apparent droplet generation was observed during wind gusts. The radar measurements were performed at 10, 20, and 45-degree incidence angles mostly at cross-wind and up-wind look geometry. Based on these measurements, we refine the previously developed Ka-band geophysical model function for high wind conditions. The droplet cloud radar signatures are apparent in the Doppler spectrum tails, but their overall contribution is rather weak. Thanks to this fact, the standard modulation transfer function (MTF) approach works well to evaluate the wave-induced Doppler velocity contribution and thus estimate the sea surface current. These results can be useful for the interpretation of tropical cyclone observation using Doppler radar techniques.

1. INTRODUCTION

Ka-band sea surface radar backscatter is now a focus of the scatterometry community because of planned Doppler scatterometer missions (Bao et al., 2017; Miao et al., 2018; Ardhuin et al., 2018; Rodriguez et al., 2019) enabling a direct estimate of the total surface currents velocity at very fine spatial resolution. Switching to the shorter but still penetrable through the atmosphere radar wavelength allows achieving the maximal possible measurement accuracy for a given antenna size (Rodriguez, 2018).

In contrast to relatively rare past Ka-band radar studies (Masuko et al., 1986; Plant et al., 1994; Walsh et al., 1998; Nekrasov and Hoogeboom, 2005), the last decade is marked with significant efforts to document the Ka-band backscattering (Ermakov et al., 2014; Boisot et al., 2015; Nouguier et al., 2016; Rodriguez et al., 2018; Marie et al., 2020) and to provide its theoretical basis (Mouche et al., 2008; Gairola et al., 2014; Fois et al., 2015; Nouguier et al., 2018). A contribution is also made by our recent studies reporting results of multi-year field Ka-band experiments from the Black Sea research platform. This latter series of research includes the parameterization of normalized radar cross-section (NRCS, Yurovsky et al., 2016), examination of its modulation by waves (Yurovsky et al., 2018a; Yurovsky et al., 2018b), and Doppler centroid modeling (Yurovsky et al., 2019).

There is one issue that has not been addressed for the Ka-band by any of these studies. For the longer C-to-Ku-band radar wavelengths, there is a clear NRCS saturation (Quilfen et al., 1998; Donnelly et al., 1999; Fernandez et al., 2006; Li et al., 2017) at wind speeds higher than 25-30 m/s that is associated with the surface drag attenuation. The Ka-band behavior at these extreme winds is unknown but is interesting for the planned Ka-band ocean radar projects. The Doppler characteristics of the signal are of special interest to understand the Doppler scatterometry potential in a wide range of environmental conditions.

The problem is also challenging because the air-sea interface at such high winds is characterized by the presence of

a spray layer above the water surface which is assumed to impact the total ocean backscatter signal especially for millimeter-scale radar wavelengths (Goldstein 1947; Plant 2003; Plant et al., 2006; Raizer 2013),

In this paper, we complement our previous radar data analyses by a case study conducted at rather strong (up to 33 m/s) wind. During wind gusts above 20...25 m/s, the generation of spray clouds was visually observed. Radar measurements made at these conditions allowed for direct assessment of the impact of sea spray on the Ka-band backscatter cross-section and Doppler velocity.

2. EXPERIMENT

The measurements presented in this study were taken from the Black Sea research platform during October, 24-25, 2018. This platform is located ~1000 m offshore of a coastal mountain canyon. At northerly winds, this canyon acts as an amplifying tunnel for a gap wind jet produced by the katabatic airflow of cold air blocked by the mountains. Such harsh conditions were observed during the experiment (Figure 1), with a 1-minute averaged wind speed reaching 33 m/s. A detailed description of the Ka-band Doppler scatterometer used in this study can be found in (Yurovsky et al., 2016). The radar data were acquired in seven records on October 24-25, 2018 (see Table 1).

Table 1. Radar record duration and look geometry.

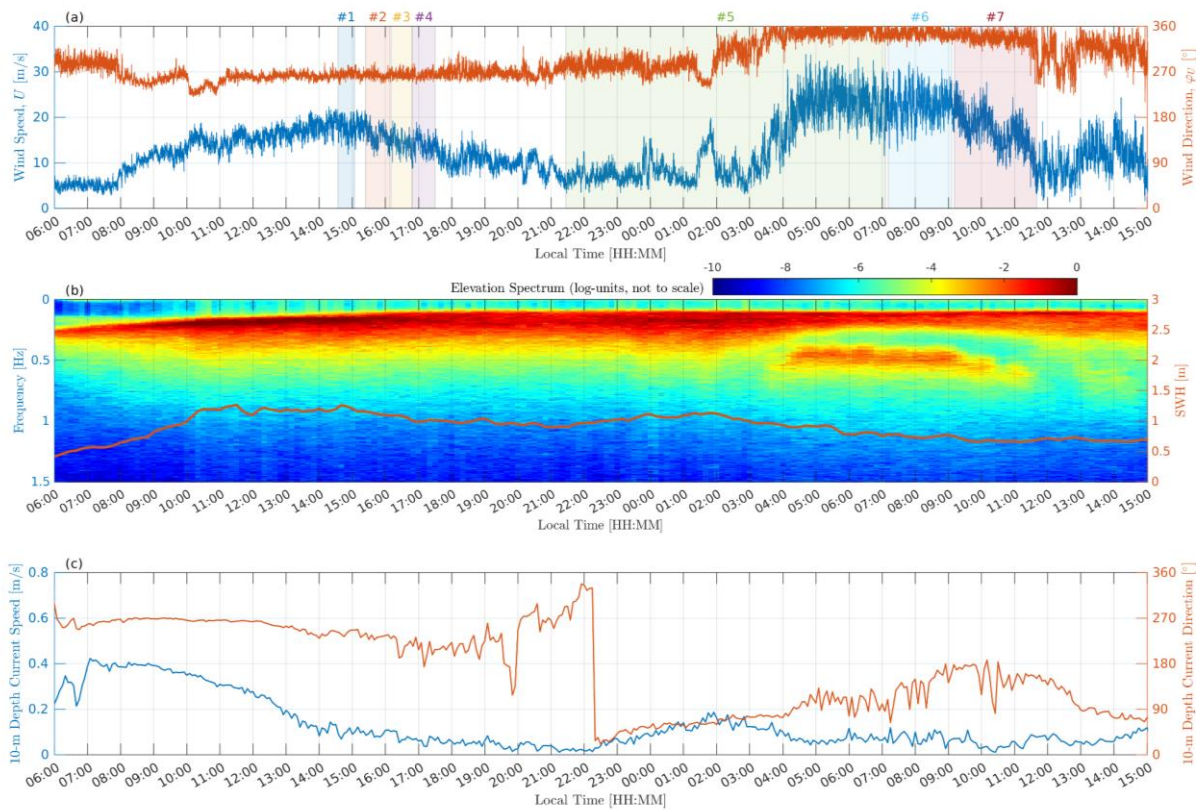| Record #	Local Time, HH:MM	Incidence angle, $\square$ [°]	Radar Azimuth, [°]	Wind speed, U, mean, (min-max) [m/s]	Mean Wind Direction, φ_U [°]
1	14:34-15:04	20	50	17.6 (11.8-21.2)	265
2	15:24-16:08	20	300	16.1 (11.3-20.6)	265
3	16:10-16:48	20	330	14.5 (10.1-19.2)	265
4	16:49-17:30	20	0	14.0 (8.8-18.9)	264
5	21:27-07:06	20	50	13.2 (3.1-33.8)	311
6	07:11-09:06	20	0	22.7 (12.5-32.1)	346
7	09:11-11:40	45	0	16.8 (3.4-28.0)	336

Figure 1. Environmental conditions during the experiment: (a) wind speed and wind direction; (b) temporal evolution of frequency wave elevation spectrum with significant wave height (SWH) overlain (red bold line, right *y*-axis); (c) current speed and current direction at 10-m depth.

Wind speed was measured by a cup anemometer installed on top of the platform mast. This 23-m height wind speed was converted to the standard 10-m height neutral wind speed using the COARE 3.0 parameterization (Fairall et al., 2003). Currents were measured by the propeller current meter submerged at the 10-m depth. Wave measurements were performed by the conductive wire wave gauges (Smolov and Rozvadovskiy, 2020; Bondur et al., 2016).

During the experiments, wind conditions were characterized by an initial period of westerly winds with wind speed varying from 10 to 20 m/s followed by an abrupt switch to strong offshore northerly winds with wind speed increasing up to 33 m/s. During the westerly wind period starting from 08:00 24-Oct., the surface wave spectrum was unimodal with significant wave height (SWH) varying from 0.8 to 1 m and a rather stable wave peak frequency of about 0.2 Hz. At these conditions, four 30-min radar records were made at incidence angle, $\theta = 20°$, and different azimuths (see Table 1, records #1-4). After 02:00 on 25-Oct., the wind direction started turning to northerly with wind speed increasing to 30 m/s. This wind transition period was fully captured by the long 9.5-hour record #5 also made at $\theta = 20°$. After the wind direction turning, the surface wave spectrum became bimodal with a residual gradually decaying 0.2-Hz swell propagating from the west and a 0.5-Hz peak corresponding to 1-km fetch-limited wind waves propagating from the north (Figure 1b). On the morning of 25-Oct., the radar look azimuth was changed to upwind (record #6). Then (record #7) the incidence angle was increased to $\theta = 45°$ (also upwind) to capture the radar backscattering during the northerly wind gradual decay period. Sea current at 10-m depth was below 0.2 m/s during the entire experiment (Figure 1c).

3. RESULTS AND DISCUSSION

3.1 Normalized Radar Cross-Section

For calm to moderate winds, $U < 15$ m/s, Doppler characteristics of Ka-band sea surface radar backscatter were discussed several times in the past studies (including those for our experimental setup, see e.g., Yurovsky et al., 2018a). Here, the focus is on Doppler radar characteristics at strong winds. Figure 2 shows instantaneous VV-polarization Doppler spectra for part of record #7 collected at $U \sim 20$ m/s offshore northerly wind. At these short-fetch wave conditions, frequent spray clouds above the sea surface were visually observed during wind gusts.
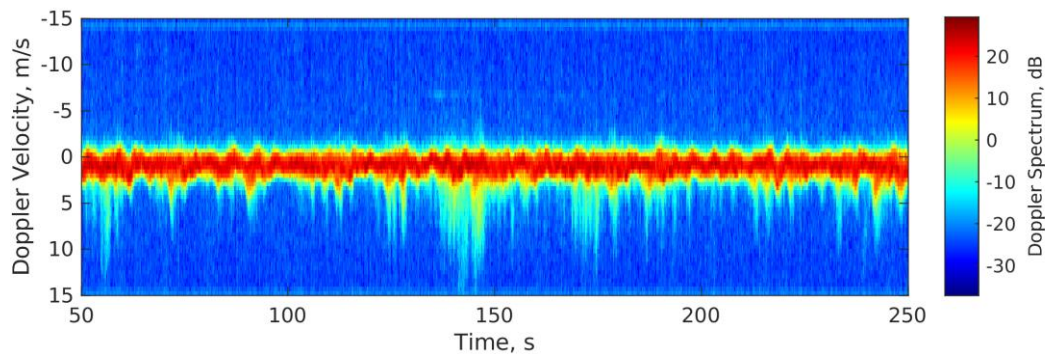

Figure 2. Sample record fragment showing VV-polarization Doppler spectrum at U ~ 20 m/s, $\theta = 45°$.

For $\theta = 20°$ (Figures 3a,b), the radar-to-wind azimuth varies in the upwind to cross-wind sector, thus both positive and somewhat weaker negative tails are present. At $\theta = 45°$ (Figures 3b,c), the radar look azimuth is predominantly upwind, thus only positive tails are present. The upper limit of resolved Doppler velocities is about 10 m/s (based on the radar signal-to-noise characteristics).

Regardless of polarization and incidence angle, the tail spectrum level corresponding to "fast" features is 3-4 orders of magnitude smaller than the peak spectrum level corresponding to "slow" features. Thus, though the spray contribution can be distinguished in the Doppler spectra due to faster propagation speed, its net NRCS contribution is negligible, at least at observed winds, $U < 35$ m/s. As a result, the mean NRCS incidence angle dependence (Figure 4) is qualitatively similar to the background Ku-band geophysical model functions (GMF) derived from TRMM (Li et al., 2017) and NSCAT4 (Wentz et al., 1999) satellite data. Interestingly, the TRMM GMF demonstrates a noticeable decrease at $U > 35$ m/s due to the wind stress saturation (Kudryavtsev, 2006). Unfortunately, our wind range is not wide enough to fully capture this feature. In general, our data are consistent with the background Ku-band GMF at $U > 10...15$ m/s. This will allow extrapolating our previous model function (KaDPMod, Yurovsky et al., 2016) to stronger winds. At lower winds, $U < 10$ m/s, our data deviate from other datasets due to complex mixed sea wave conditions typical of the Black Sea.
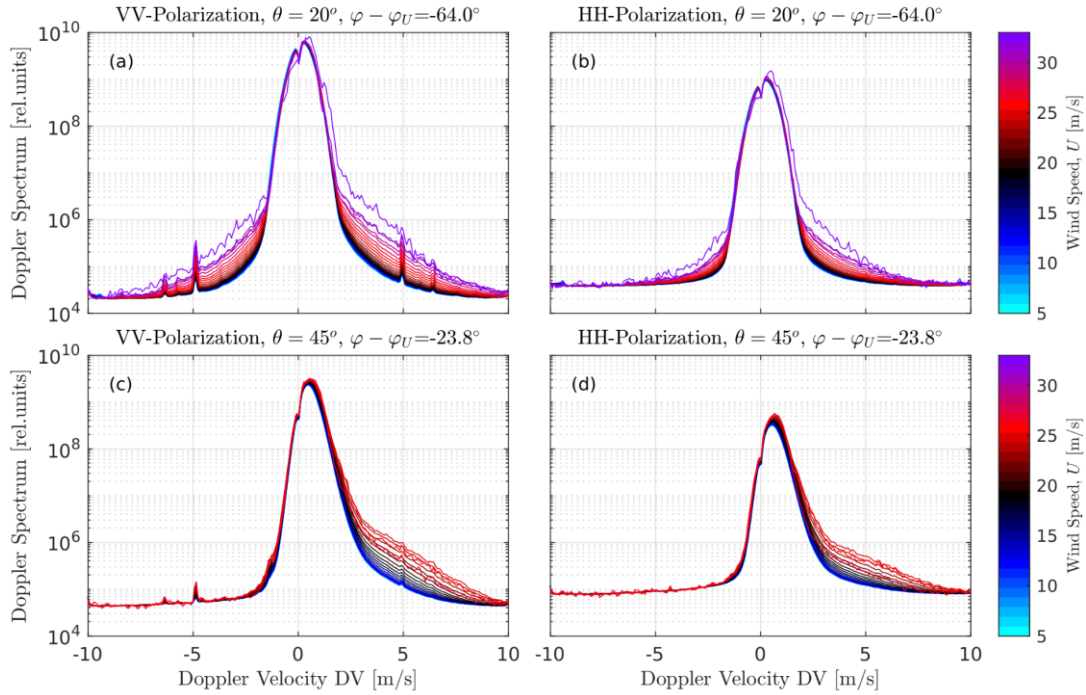
Figure 3. Doppler spectra averaged at different color-coded wind speeds for (a,b) $\theta = 20°$ and (c,d) $\theta = 45°$. Left column – VV-polarization, right column – HH-polarization.
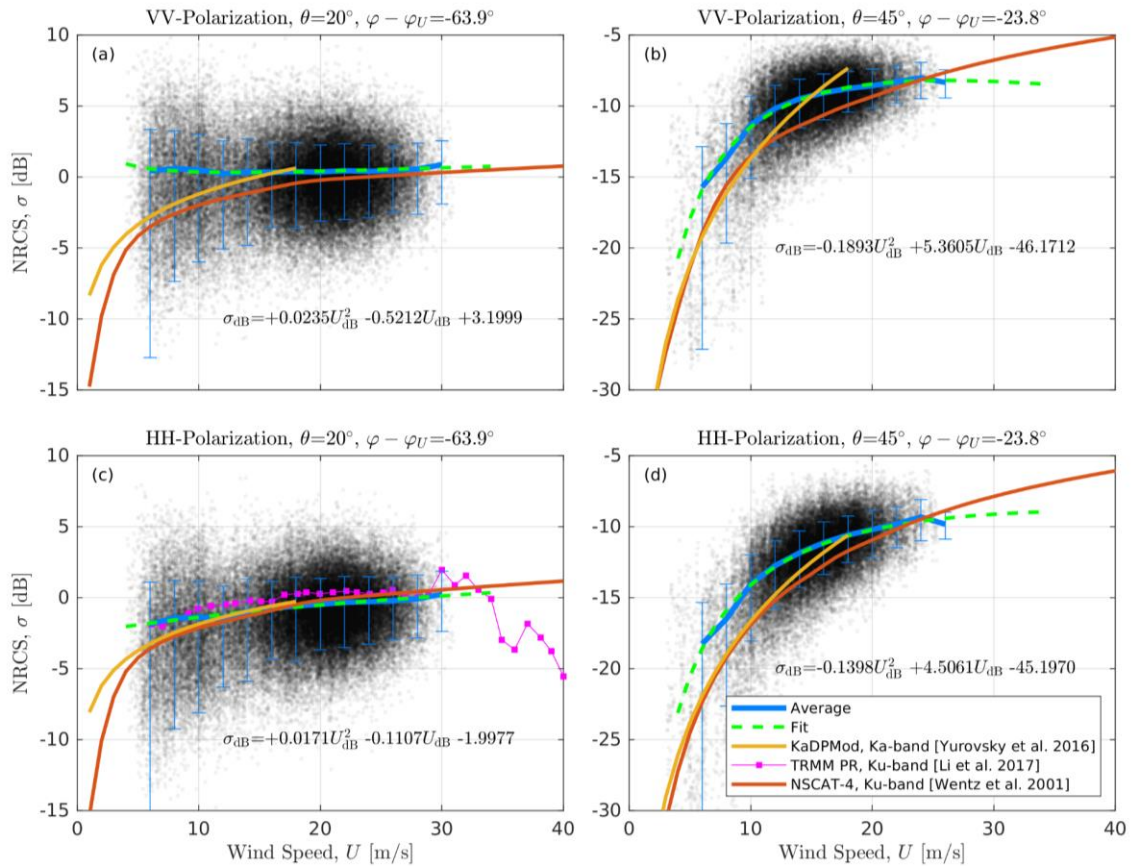

Figure 4. Measured NRCS for (a,c) $\theta = 20°$ and (b,c) $\theta = 45°$ in comparison with KaDPMod, NSCAT-4, and TRMM GMFs. (a,b) – VV-polarization, (c,d) – HH-polarization.

3.2 Doppler Centroid Velocity

We consider the Doppler spectrum centroid as a parameter for sea surface current velocity retrieval. From the raw data, the instantaneous Doppler spectra (Figure 2), $S(f_D,t)$, can be estimated as a function of Doppler frequency, f_D, and time, t. Then the instantaneous Doppler centroid (DC) velocity, V_D,

$$V_D(t) = \frac{\int f_D S(f_D,t) df_D}{\int S(f_D,t) df_D}. \tag{1}$$

The DC reflects the instantaneous kinematics of the surface within a few meter wide radar footprint which size is normally smaller than the typical peak wavelength for the majority of observed conditions. The DC of the time-averaged spectrum,

$$V_D = \frac{\iint f_D S(f_D,t) df_D dt}{\iint S(f_D,t) df_D dt}, \tag{2}$$

is a proxy for Doppler measurement from a satellite or an airborne sensor, with a kilometer-wide footprint spanning many dominant wavelengths.

The 1-min average V_D for all records corrected for the contribution from the surface currents (estimated from 10-m current measurements) is shown in Figure 5 versus the line-of-sight wind vector projection, $U\sin\theta\cos(\varphi-\varphi_U)$. There is a clear correlation of DC with this wind projection which is caused by the direct relationship between wind and waves (Chapron et al., 2005). First, there are two data point clouds with differing slopes corresponding to $\theta = 45°$ (record #7, dark red) and $\theta = 20°$ (other records). Second, there is a change in the slope within data points from record #5 associated with an abrupt change in wind speed and direction between 01:00 and 02:00 on 25-Oct (Figure 1) at virtually constant wave direction (Figure 5, record #5, green, negative DC area).
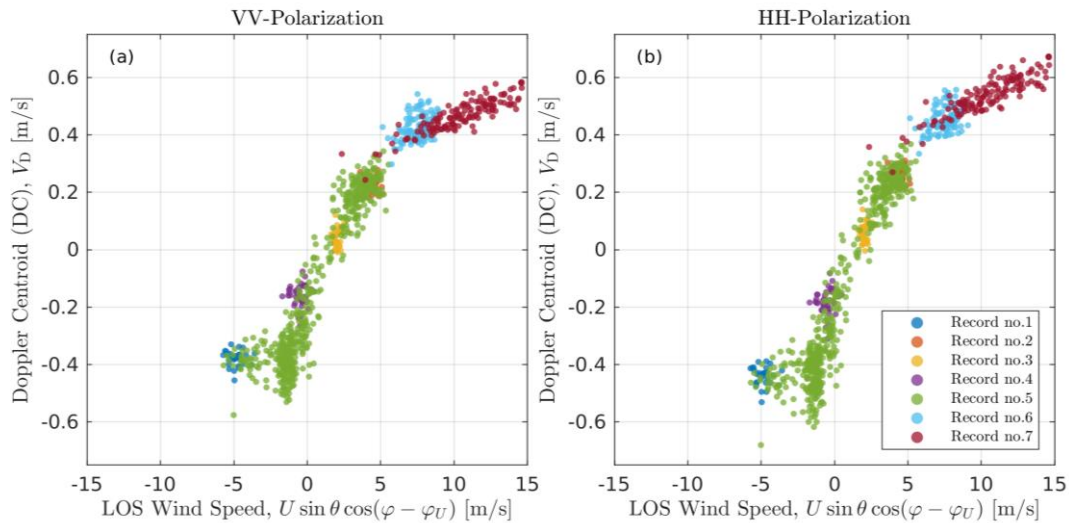

Figure 5. Measured Doppler centroid (DC) versus wind speed line-of-sight (LOS) projection for (a) VV-polarization and (b) HH-polarization. The color indicates the run number (see Figure 1 and Table 1). Dashed lines show Bragg wave phase speed for $\theta = 20°$ and $\theta = 45°$.

3.3 Wave-Induced Doppler Velocity

To get deeper insights into the Doppler imaging mechanism, the Doppler centroid is shown separately for two characteristic records. Record #5 (Figure 6) is remarkable due to the fully recorded wind direction turn event, with short interruptions during two rain events. During its first part, $t < 200$ min, the combined DC contribution from the background current, Bragg velocity, and wind drift (~1.5% U, Yurovsky et al., 2019) is ~25% of the total DC (Figure 6a, green and blue lines). Hence, the remaining 75% is produced by the wave-induced Doppler velocity (WIDV). After the wind direction turn, the partitioning changes to ~50/50% due to the change in wave regime. Notice that current+drift+Bragg contribution changes its sign but its magnitude remains ~0.1 m/s. The wave-induced Doppler velocity (WIDV) contribution (estimated as the difference between the total measured DC and the
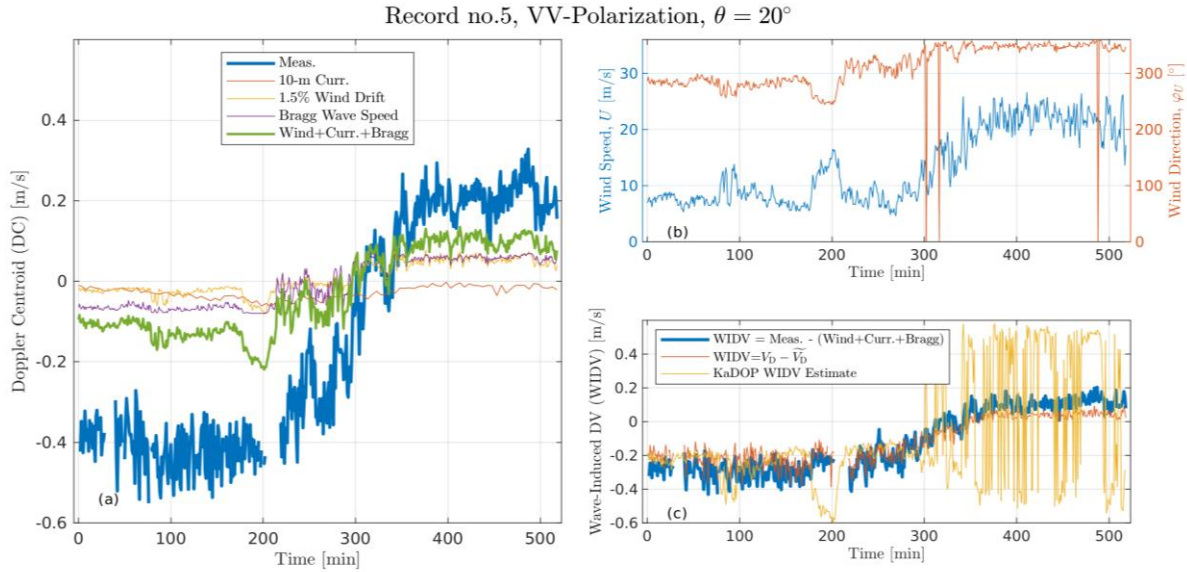
Record no.5, VV-Polarization, $\theta = 20°$

Figure 6. Time series of 1-min average: (a) Doppler centroid (DC) and its contribution due to currents, wind, and Bragg scattering, (b) wind speed and wind direction, and (c) wave-induced Doppler velocity (WIDV) estimated in different ways. Record #5 ($\theta = 20°$, see Figure 1, Table 1).

sum of background current, wind drift, and Bragg velocity) is shown in Figure 6c by the blue line. An alternative estimate of WIDV (calculated as the difference between $V_D - \tilde{V_D}$) is consistent with the former estimate but has a smaller magnitude because $V_D - \tilde{V_D}$ accounts only for waves resolved by the radar footprint.

As demonstrated, the WIDV is the dominant part of the DC. Thus, inverting the DC into the surface current requires precise knowledge of the WIDV. Using the present dataset, we test the previously developed KaDOP model which is essentially the WIDV model (Yurovsky et al. 2019). The KaDOP-based estimate (Figure 6c, yellow line) is somewhat less than the measurements for the westerly-wind part (Figure 6c, $t < 200$ min) but overestimates the measurements during wind gusts (Figure 6c, $t \sim 200$ min,). This suggests that the fully developed (Pierson and Moskowitz, 1964) wave spectrum parameterization as a function of wind speed (used in the KaDOP model) does not describe well the spectrum observed in the present experiment, especially during abrupt wind changes.

Part of the record acquired at northerly-wind ($t > 300$ min) is characterized by a strong scatter of KaDOP-based DC estimates around the mean level that roughly corresponds to measured DC values. That strong DC scatter is explained by the radar modulation transfer function (MTF) features. There are two regions in 2-D incidence angle – radar azimuth, (θ, φ)-domain, where a particular MTF component magnitude may be zero. For the tilt component, $M(\theta, \varphi)$, it occurs at $\varphi = 90°$ where cross-look tilts don't cause any radar backscatter response. For the hydrodynamics component, it occurs in the so-called contrast inversion zone at small incidence angles, $\theta = 10...20°$, where the backscatter magnitude doesn't depend on small-scale surface roughness. Contrast inversion zone θ-location depends on the sea surface roughness (mean square slope) and thus on wind speed. The intersection of these two areas corresponds to a special point in the (θ, φ)-domain where wave-induced radar backscatter modulations vanish. KaDOP empirical MTF function (Figure 7) has this special point but at a smaller azimuth,
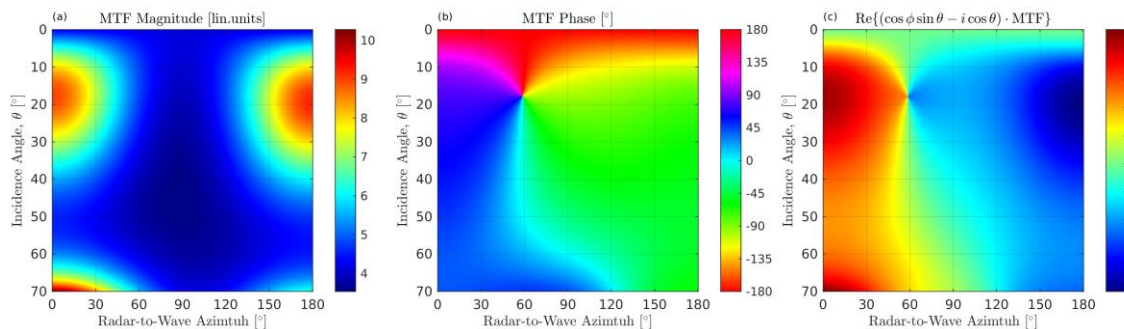

Figure 7. The KaDOP modulation transfer function (MTF) (a) magnitude, (b) phase, and (c) non-scaled contribution to the wave-induced Doppler velocity (WIDV) versus radar-to-wave azimuth and incidence angle at 10 m/s wind speed and VV-polarization.

$\varphi \sim 60°$, possibly due to empirical fitting errors. Accidentally, the look geometry during the northerly wind part of record #5 is very close to this special point. At these conditions, even small variations in wind azimuth may lead to large deviations in WIDV estimates (see Figure 7c showing the unscaled WIDV contribution computed from the MTF). If the MTF is applied to the real finite-width spectrum, this special point is smoothed and no artifacts appear in estimated DV values. But when the uni-directional spectrum parameterization is used, the results of DV retrieval should be interpreted with caution.

With the incidence angle increase to $\theta = 45°$ (record #7, Figure 8), the DC increases up to ~0.6 m/s due to increasing the line-of-sight projection factor, $\sin\theta$. The gradual wind decay observed during record #7 is accompanied by the corresponding DC decay. Yet, the $1.5\% U$ wind drift parameterization is not sufficient to fully predict the DC (Figure 8a, green and blue lines). The total WIDV (Figure 8c) is smaller than for $\theta = 20°$ because of the weaker modulation magnitude (Figure 7a). The long-wave WIDV estimate, $V_D - \tilde{V}_D$, is almost zero because the dominant 0.5-Hz fetch-limited waves are not resolved by the radar footprint. The swell is also presented in the scene (Figure 1) but comes obliquely to the radar look direction and thus does not affect the DC significantly. The KaDOP prediction this time is more reliable at stronger wind speed, $U = 15...20$ m/s, but overestimates the measurements at weaker winds. However, in this more slanted look geometry, the WIDV is not so important because the DC is mostly governed by the sum of drift current and Bragg contribution.
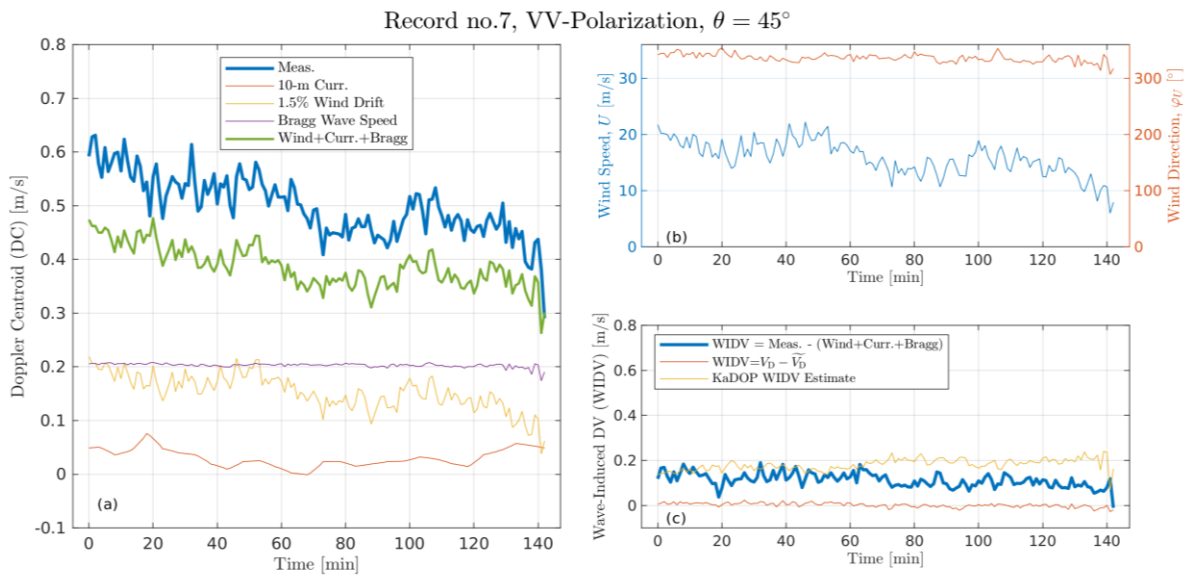

Figure 8. The same as Figure 6 but for record #7 ($\theta = 45°$, see Figure 1, Table 1).

5. SUMMARY

We present field measurements of the Ka-band cross-section and Doppler shift at rather strong (up to 33 m/s) wind speed with distinct events of spray formation above the sea surface. Water droplet propagation within a radar beam causes volume scattering and high-frequency signatures in the radar Doppler spectrum with Doppler velocities up to 10 m/s. However, their spectral energy is 3 to 4 orders of magnitude weaker than the spectral energy of the signal backscattered from the sea surface. Thus, the spray contribution to the total NRCS, observed in our experiment, is negligible.

The same result holds for the Doppler spectrum centroid which is also dominated by the slow surface rather than the fast volume scattering. With several long records in hand, we demonstrate how the conventional radar modulation transfer function (MTF) approach adopted for the Doppler centroid estimation (e.g., in the KaDOP model of Yurovsky et al., 2019) can be applied to changing wind and wave environments. On average, the KaDOP model adequately represents sea surface radar measurements. But, the effect of rapid changes in winds can not be represented well by this model due to the utilization of a wind-based parameterization for the surface wave spectrum (e.g., Pierson-Moskowitz, 1964).

Another important issue is the MTF specific point corresponding to the intersection of zero tilt modulation (cross-wave) and zero hydro-dynamics modulation (contrast inversion at small incidence angles) areas. At this critical point, the wave-induced Doppler velocity turns to zero. If a unidirectional wave spectrum approximation is used, then small variations of wave (wind) azimuth around this point may significantly increase the scatter of DC

predictions. This feature is indeed an artifact because the real wave spectrum always has finite azimuth width that smooths the DC around this critical point.

Our present findings confirm that DC prediction depends primarily on adequate knowledge of wave rather than wind parameters. In contrast to traditional NRCS geophysical model functions that solely rely on wind speed for sea state representation, the DC modeling is expected to be more robust if wave information is directly used.

ACKNOWLEDGMENT

REFERENCES

Ardhuin, F., Aksenov, Y., Benetazzo, A., Bertino, L., Brandt, P., Caubet, E., Chapron, B., Collard, F., Cravatte, S., Dias, F., Dibarboure, G., Gaultier, L., Johannessen, J., Korosov, A., Manucharyan, G., Menemenlis, D., Menendez, M., Monnier, G., Mouche, A., Nouguier, F., Nurser, G., Rampal, P., Reniers, A., Rodriguez, E., Stopa, J., Tison, C., Tissier, M., Ubelmann, C., van Sebille, E., Vialard, J., Xie, J., 2018. Measuring currents, ice drift, and waves from space: the Sea Surface KInematics Multiscale monitoring (SKIM) concept. Ocean Science, 14, pp. 337–354.

Bao, Q., Lin, M., Zhang, Y., Dong, X., Lang, S., Gong, P., 2017. Ocean surface current inversion method for a doppler scatterometer. IEEE Trans. Geosci. Remote Sens., 55(11), pp. 6505–6516.

Boisot, O., Pioch, S., Fatras, C., Caulliez, G., Bringer, A., Borderies, P., Lalaurie, J.-C., Guérin, C.-A., 2015. Ka-band backscattering from water surface at small incidence: A wind-wave tank study. J. Geophys. Res. (Oceans), 120, pp. 3261–3285.

Bondur, V. G., Dulov, V. A., Murynin, A. B., Yurovsky, Y. Y., 2016. A study of sea-wave spectra in a wide wavelength range from satellite and in-situ data. Izvestiya, Atmospheric and Oceanic Physics, 52(9), pp.888–903.

Chapron, B., Collard, F., Ardhuin, F., 2005. Direct measurements of ocean surface velocity from space: Interpretation and validation. J. Geophys. Res. (Oceans), 110, 7008.

Donnelly, W. J., Carswell, J. R., McIntosh, R. E., Chang, P. S., Wilkerson, J., Marks, F., Black, P. G., 1999. Revised ocean backscatter models at C and Ku band under high-wind conditions. J. Geophys. Res. (Oceans), 104, pp. 11485–11498.

Ermakov, S. A., Kapustin, I. A., Kudryavtsev, V. N., Sergievskaya, I. A., Shomina, O. V., Chapron, B., Yurovskiy, Y. Y., 2014. On the doppler frequency shifts of radar signals backscattered from the sea surface. Radiophysics and Quantum Electronics, 57(4), pp. 239–250.

Fairall, C. W., Bradley, E. F., Hare, J. E., Grachev, A. A., Edson, J. B., 2003. Bulk Parameterization of Air Sea Fluxes: Updates and Verification for the COARE Algorithm. Journal of Climate, 16, pp. 571–591.

Fernandez, D. E., Carswell, J. R., Frasier, S., Chang, P. S., Black, P. G., Marks, F. D., 2006. Dual-polarized C- and Ku-band ocean backscatter response to hurricane-force winds. J. Geophys. Res. (Oceans), 111, C08013.

Fois, F., Hoogeboom, P., Le Chevalier, F., Stoffelen, A., 2015. An analytical model for the description of the full-polarimetric sea surface doppler signature. J. Geophys. Res. (Oceans), 120(2), pp. 988–1015.

Gairola, R. M., Prakash, S., Mahesh, C., Gohil, B. S., 2014. Model Function for Wind Speed Retrieval from SARAL-AltiKa Radar Altimeter Backscatter: Case Studies with TOPEX and JASON Data. Marine Geodesy, 37(4), pp. 379–388.

Goldstein, H., 1947. Sea Echo. In: Propagation of Short Radio Waves, edited by Kerr, D. E., Peter Peregrinus Ltd., London, pp. 481–571.

Kudryavtsev, V. N., 2006. On the effect of sea drops on the atmospheric boundary layer. J. Geophys. Res. (Oceans), 111, C07020, doi: 10.1029/2005JC002970.

Li, X., Zhang, B., Mouche, A., He, Y., Perrie, W., 2017. Ku-Band Sea Surface Radar Backscatter at Low Incidence Angles under Extreme Wind Conditions. Remote Sens., 9(5), 474.

Marié, L., Collard, F., Nouguier, F., Pineau-Guillou, L., Hauser, D., Boy, F., Méric, S., Peureux, C., Monnier, G., Chapron, B., Martin, A., Dubois, P., Donlon, C., Casal, T., Ardhuin, F., 2020. Measuring ocean surface velocities with the KuROS and KaRADOC airborne near-nadir Doppler radars: a multi-scale analysis in preparation of the

SKIM mission. Ocean Science, 16, pp. 1399–1429.

Masuko, H., Okamoto, K., Shimada, M., Niwa, S., 1986. Measurement of microwave backscattering signatures of the ocean surface using X band and Ka band airborne scatterometers. J. Geophys. Res. (Oceans), 91, pp. 13065–13084.

Miao, Y., Dong, X., Bao, Q., Zhu, D., 2018. Perspective of a Ku-Ka Dual-Frequency Scatterometer for Simultaneous Wide-Swath Ocean Surface Wind and Current Measurement. Remote Sens., 10(7), 1042.

Mouche, A. A., Chapron, B., Reul, N., Collard, F., 2008. Predicted doppler shifts induced by ocean surface wave displacements using asymptotic electromagnetic wave scattering theories. Waves in Random Media, 18(1), pp. 185–196.

Nekrasov, A., Hoogeboom, P., 2005. A Ka-Band Backscatter Model Function and an Algorithm for Measurement of the Wind Vector Over the Sea Surface. IEEE Geosci. Remote Sens. Lett., 2(1), pp.23–27.

Nouguier, F., Chapron, B., Collard, F., Mouche, A., Rascle, N., Ardhuin, F., Wu, X., 2018. Sea surface kinematics from near-nadir radar measurement. IEEE Trans. Geosci. Remote Sens., 56(10), pp. 6169–6179.

Nouguier, F., Mouche, A., Rascle, N., Chapron, B., Vandemark, D., 2016. Analysis of Dual-Frequency Ocean Backscatter Measurements at Ku- and Ka-Bands Using Near-Nadir Incidence GPM Radar Data. IEEE Geosci. Remote Sens. Lett., 13(9), pp. 1310–1314.

Pierson, W.J., Moskowitz, L., 1964. A proposed spectral form for fully developed wind seas based on the similarity theory of S. A. Kitaigorodskii. J. Geophys. Res., 69, pp. 5181–5190.

Plant, W. J., 2003. Microwave sea return at moderate to high incidence angles. Waves in Random Media, 13, pp. 339–354.

Plant, W. J., Keller, W. C., Asher, W. E., 2006. Is Sea Spray a Factor in Microwave Backscatter from the Ocean? In 2006 IEEE MicroRad, pp. 115–118.

Plant, W. J., Terray, E. A., Petitt, R. A., Keller, W. C., 1994. The dependence of microwave backscatter from the sea on illuminated area: Correlation times and lengths. J. Geophys. Res. (Oceans), 99, pp. 9705–9723.

Quilfen, Y., Chapron, B., Elfouhaily, T., Katsaros, K., Tournadre, J., 1998. Observation of tropical cyclones by high-resolution scatterometry. J. Geophys. Res. (Oceans), 103(C4), pp. 7767–7786.

Raizer, V., 2013. Radar backscattering from sea foam and spray. In Proceedings of International Geoscience and Remote Sensing Symposium, 21-26-Jul 2013, Melbourne, Australia, pp. 4054–4057.

Rodriguez, E., 2018. On the Optimal Design of Doppler Scatterometers. Remote Sens., 10(11), 1765.

Rodriguez, E., Wineteer, A., Perkovic-Martin, D., Gál, T., Stiles, B.W., Niamsuwan, N., Rodriguez Monje, R., 2018. Estimating Ocean Vector Winds and Currents Using a Ka-Band Pencil-Beam Doppler Scatterometer. Remote Sensing, 10(4), 576.

Rodriguez, E., Bourassa, M., Chelton, D., Farrar, J. T., Long, D., Perkovic-Martin, D., Samelson, R., 2019. The Winds and Currents Mission Concept. Frontiers in Marine Science, 6, 438.

Smolov, V. E., Rozvadovskiy, A. F., 2020. Application of the Arduino Platform for Recording Wind Waves. Physical Oceanography, 27(4), pp. 430–441.

Walsh, E. J., Vandemark, D. C., Friehe, C. A., Burns, S. P., Khelif, D., Swift, R. N., Scott, J. F., 1998. Measuring sea surface mean square slope with a 36-GHz scanning radar altimeter. J. Geophys. Res. (Oceans), 103(C6), pp. 12587–12601.

Wentz, F., Smith, D., 1999. A model function for the ocean normalized radar cross section at 14 GHz derived from NSCAT observations. J. Geophys. Res. (Oceans), 104 (C5), pp. 11499-11514.

Yurovsky, Yu. Yu., Kudryavtsev, V. N., Grodsky, S. A., Chapron, B., 2016. Ka-Band Dual Copolarized Empirical Model for the Sea Surface Radar Cross Section. IEEE Trans. Geosci. Remote Sens., 55(3), pp. 1629–1647.

Yurovsky, Yu. Yu., Kudryavtsev, V. N., Chapron, B., Grodsky, S. A., 2018a. Modulation of Ka-band Doppler Radar Signals Backscattered from the Sea Surface. IEEE Trans. Geosci. Remote Sens., 56(5), pp. 2931 – 2948.

Yurovsky, Yu. Yu., Kudryavtsev, V. N., Grodsky, S. A., Chapron, B., 2018b. Low-Frequency Sea Surface Radar Doppler Echo. Remote Sens., 10(6), 870.

Yurovsky, Yu. Yu., Kudryavtsev, V. N., Grodsky, S. A., Chapron, B., 2019. Sea Surface Ka-Band Doppler Measurements: Analysis and Model Development. Remote Sensing, 11(7), 839.